Lab on a Chip

Supporting Information

Microreactor designed for efficient plasma-liquid segmented flows

Pierre Dedieu, Gabriel Morand, Karine Loubière, Stéphanie Ognier*, Michael Tatoulian

Contents

1 ITO deposition process

ITO electrodes were deposited on the reactor using the hybrid magnetron sputtering (HSPT520, Plasmionique Inc.) from Institut Pierre Gilles de Gennes clean room. Prior to ITO deposition, the reactor surface was cleaned with an oxygen/argon plasma at 50 W for 5 min (5 mTorr, $Q_{Ar} = 2\ Q_{O_2} = 20$ mL min^{-1}, substrate holder rotating at 5 rpm). The atmosphere was replaced by pure argon flowing at 30 mL min^{-1} at a pressure of 9 mTorr. The deposition process started with a pre-sputtering step where ITO target power was slowly increased from 15 W to 50 W at 5 W min^{-1} while maintaining the target shutter closed. This step aimed at eliminating target pollution and avoiding thermal stress on the target. Once at 50 W, the target shutter was opened for a deposition time of 10 min (substrate holder rotating at 5 rpm, substrate to target distance of 30 mm). After ITO target temperature decrease and chamber pressurising, the process was repeated to deposit an electrode on the other side of the reactor. After deposition of both electrodes, the reactor was submitted to a thermal treatment at 400 °C for 2 h. After thermal annealing, the thickness of the electrodes was 50 nm and the transmittance of the electrodes was 90 % at 493 nm, while the resistivity of the electrodes was measured to 1.0 ± 0.1 kΩ/cm.

2 Lissajous method for plasma power measurements

The instantaneous power in the reactor p(t) can be expressed as a function of the voltage applied to the reactor $u_r(t)$ and the current that goes through it $i_r(t)$:

$$p(t) = u_r(t) \cdot i_r(t) \tag{SI.1}$$

A high voltage supply, comprising a low frequency generator (RS Pro AFG-21025) and a voltage amplifier (Trek-10/40A-HS), was connected to the electrodes. To measure the electrical current in the circuit, a capacitor with capacity C = 153 nF was placed in series with the reactor, as shown in Figure SI.1(a). Voltage and intensity were monitored using a PicoScope 3205D and the PicoScope 6 software. As the reactor capacity was around 150 pF, it could be assumed negligible. Thus the electrical current could be calculated by measuring the voltage on the capacitor $u_c(t)$:

$$i_r(t) = C\frac{du_c(t)}{dt} \tag{SI.2}$$

The voltage on the capacitor varied from 1 V to 30 V and was considered negligible compared to the voltage applied to the reactor, which was therefore approximated to the voltage delivered by the amplifier $u_a(t)$. The plasma power P was measured by averaging the temporary power over a period of the sinusoidal voltage T[1]:

$$P = \frac{1}{T}\int_0^T u_r(t)i_r(t)dt = \frac{1}{T}\int_0^T u_a(t)du_c(t) \tag{SI.3}$$

The plot of $u_c(t)$ as a function of $u_a(t)$ is called a Lissajous plot and allows to visualize when the plasma breakdown occurs. Figures SI.1(b) and SI.1(c) show an example of a Lissajous plot before and after plasma generation respectively. The breakdown voltage was measured by slowly increasing the voltage until the Lissajous plot shape changed.
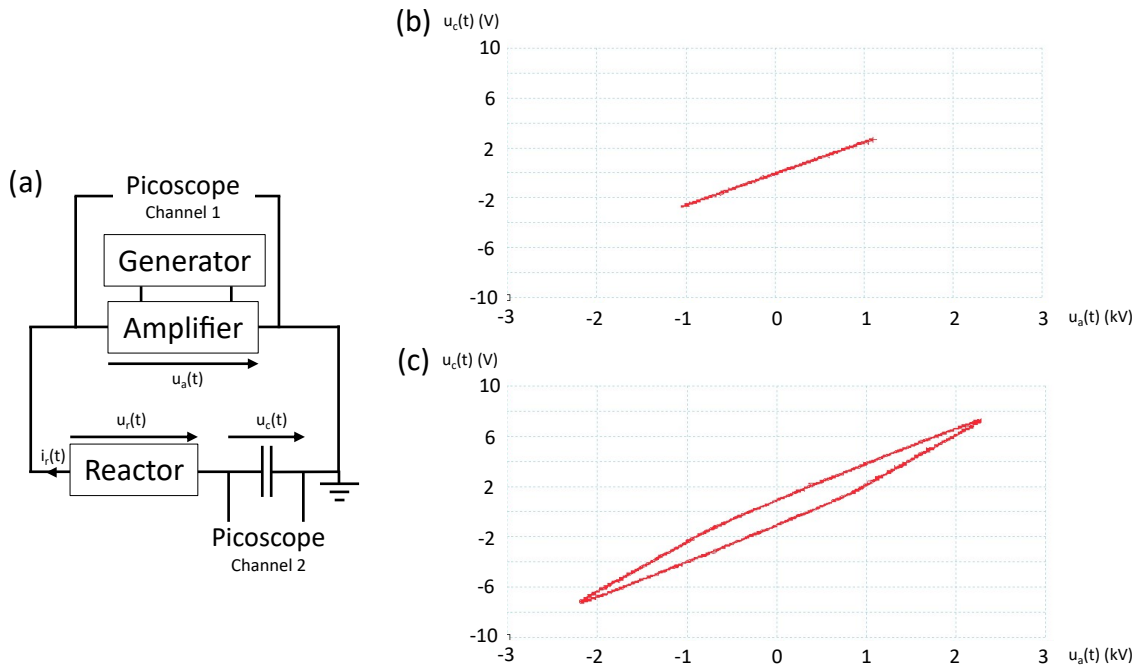

Fig. SI. 1 Electrical setup used for plasma experiments (a) and Lissajous plot before (b) and after (c) plasma breakdown in the reactor.

3 RTD experiments

The setup used for residence time distribution (RTD) experiments is shown in Figure SI.2. A 2x2 ways rotary valve was connected to the reactor liquid inlet, to syringes containing pure ethanol and a $5 \ 10^{-2}$ mol L^{-1} methylene blue (MB) solution in ethanol respectively, and to a collecting beaker. A segmented flow was first generated with argon and pure ethanol, and let to stabilize for ten residence times. The valve was then turned (Figure SI.2a') to introduce MB in the reactor with a profile close to a step (Figure SI.4a). An optical fiber connected to a Maya Pro 2000 spectrometer was placed at the inlet and outlet of the reactor and measured transmitted light intensity at 493.1 nm, corresponding to the transmission maximum, as a function of time (Figure SI.2b).
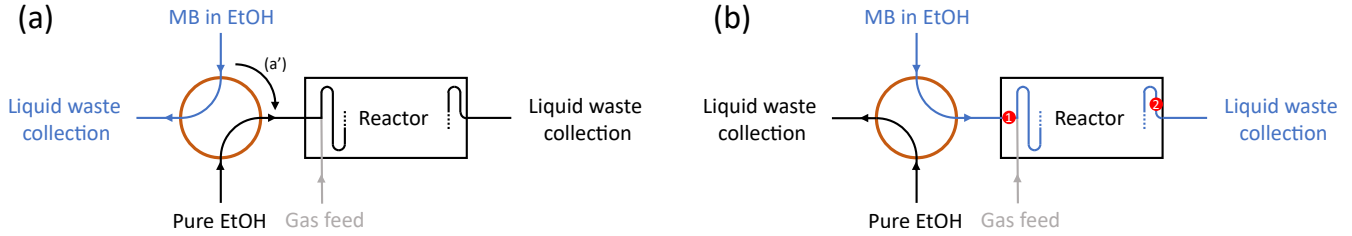

Fig. SI. 2 Experimental setup used for RTD experiments before (a) and after (b) MB injection, triggered by rotating a 2x2 ways valve (a'). An optical fiber was placed at positions symbolized by red circles before the T-junction and at the outlet of the reactor.

The evolution of MB concentration over time right after the T-junction is described in Figure SI.3. After stabilisation of the argon-ethanol segmented flow, both slugs and the liquid film were composed of pure ethanol (Figure SI.3a). When the MB solution reached the T-junction, it was hypothesized that MB was introduced in the slugs while the liquid film remained constituted of pure ethanol. The liquid film was progressively saturated in MB by diffusion during contact with the liquid slugs (Figure SI.3b-c). At the equilibrium, namely $t_{red} \gg 1$, the MB concentration in slugs and the liquid film was homogeneous (Figure SI.3d).
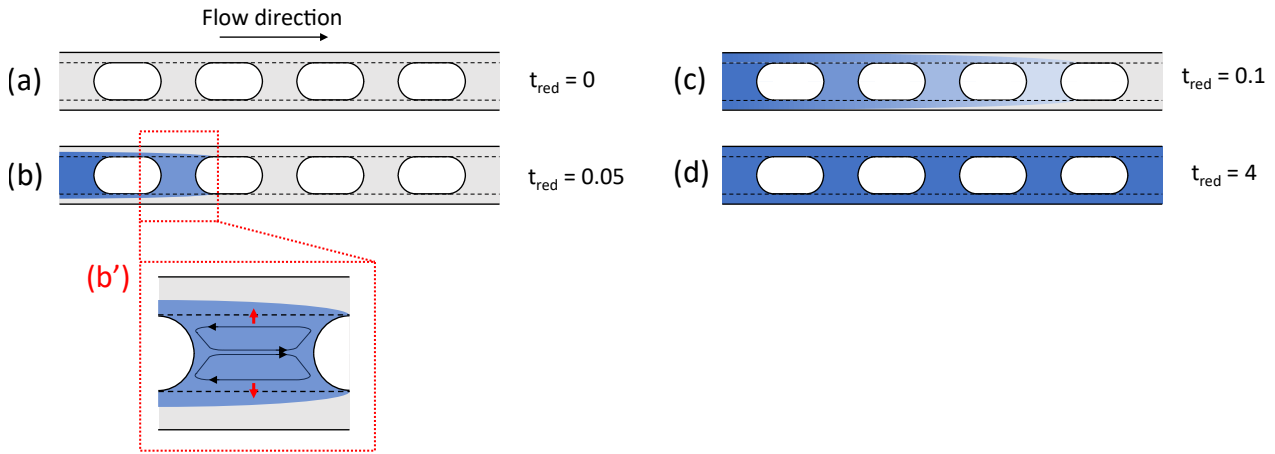

Fig. SI. 3 Schematical representation of MB concentration evolution in an argon-ethanol segmented flow right after the T-junction for different reduced times after the MB solution reached the T-junction (a-d). The different transport mechanisms of MB, namely recirculation in the liquid slug (black arrows) and diffusion from the slug to the liquid film (red arrows) are represented in the insert (b'). Grey: pure ethanol, white: gas, blue scale: MB concentration, black dotted line: slug-film interface.

Figure SI.4 shows typically observed transmitted light intensity profiles. Figure SI.4a evidences the MB concentration profile at the inlet of the reactor is indeed a step. The time resolution of the spectrometer was 6 ms and was precise enough to see bubbles and slugs flow at the outlet of the reactor (Figure SI.4b and insert). To obtain the RTD from the transmitted light intensity measurements, the intensity was averaged over each slug and bubble and derivated against time. The derivative was normalized to 1 and reduced time t_{red} was computed by normalizing liquid residence time to bubble residence time. Negative t_{red} corresponded to moments when the MB solution had not reached the T-junction yet. The evolution of normalized intensity derivative as a function of t_{red} was fitted to a Villermaux model[2] (Figure SI.4c, Equation (SI.4)) :

$$E(t_{red}) = a\sqrt{\frac{1}{t_{red}}}exp[-\frac{b}{t_{red}}(t_{red} - \theta)^2]$$

(SI.4)

with a, b and θ the variables of the numerical fit. The mean reduced time θ was approximated to the reduced time corresponding to the maximum intensity derivative. The distributions obtained showed the characteristic shape for gas-liquid segmented flows, with a sharp increase at the mean reduced time and a long tail. The broadening of the distribution and the length of the tail depended on fluidic conditions (Figure SI.4d).
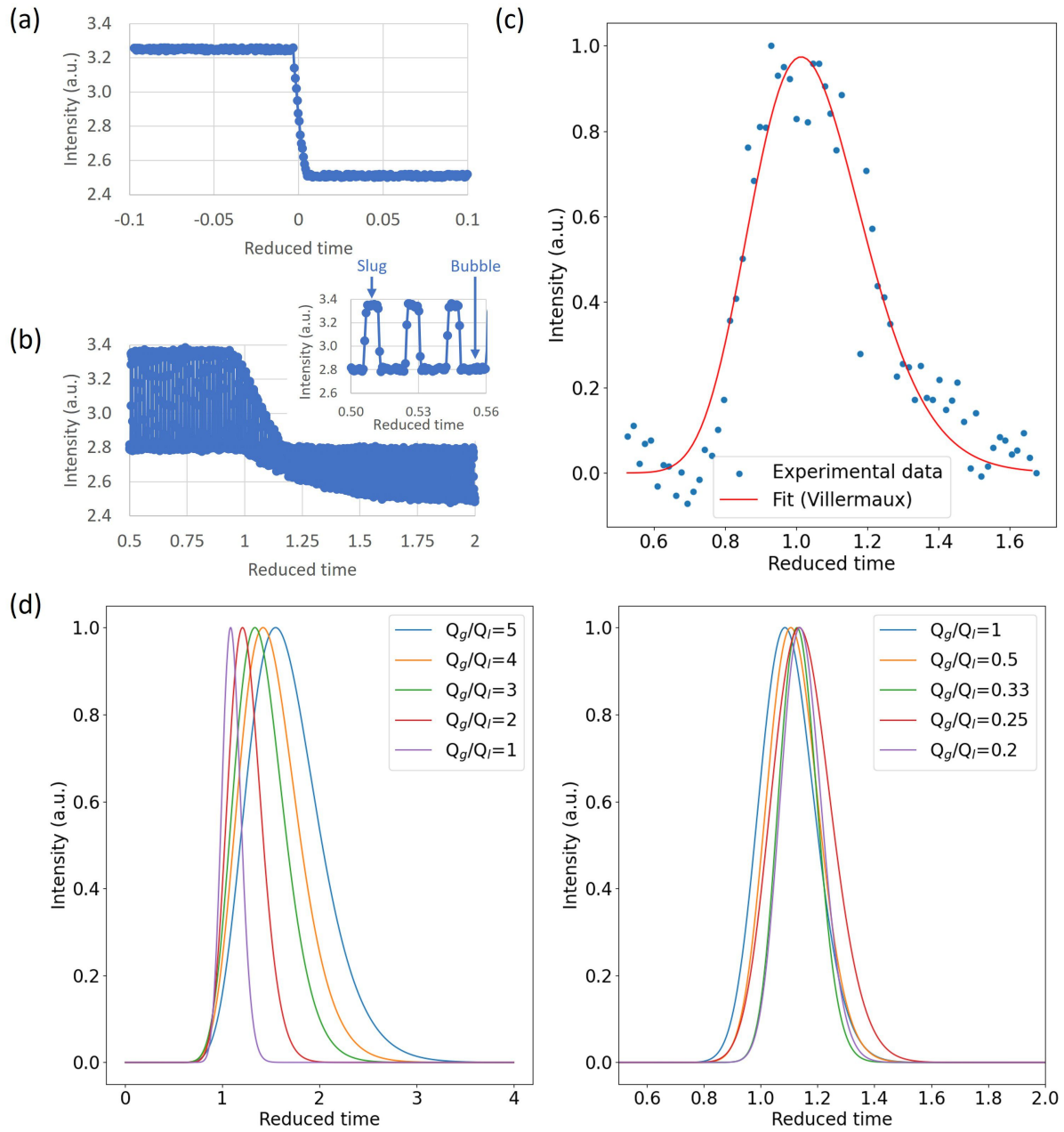
Fig. SI. 4 Typically observed transmitted light intensity profiles observed before the T-junction (a) and at the outlet of the reactor (b), with signal attribution to bubbles and slugs flowing (b, insert). Transmitted light intensity derived against time was fitted to a Villermaux model (c), yielding the evolution of the residence time distribution depending on fluidic conditions (d).

During the RTD experiments, it was noticed that the transmitted intensity of bubbles decreased after MB injection (Figure SI.5a). This variation was attributed to the presence of MB in the liquid film. Using the geometrical repartition of the liquid film shown in Figure SI.5b, a mean film thickness δ was calculated using Equation (SI.5):

$$\delta = h \frac{\Delta I_b}{\Delta I_s} \qquad \text{(SI.5)}$$

with h the channel height, ΔI_b and ΔI_s the difference of transmitted light intensities with pure ethanol and with MB in ethanol averaged over bubbles and slugs respectively at $t_{red} \gg 1$. However, it should be noted that the geometrical model used (Figure SI.5b) is approximate and the actual liquid film repartition in the microchannel is more complex due to the trapezoidal shape of the microchannel cross-section. In particular, the film should probably be thicker in the corners than in the sides, and with different thicknesses between the vertical and horizontal wall sides (Figure SI.5c). The theoretical correlations for film thickness on the reactor walls are therefore expected not to fit with experimental values.
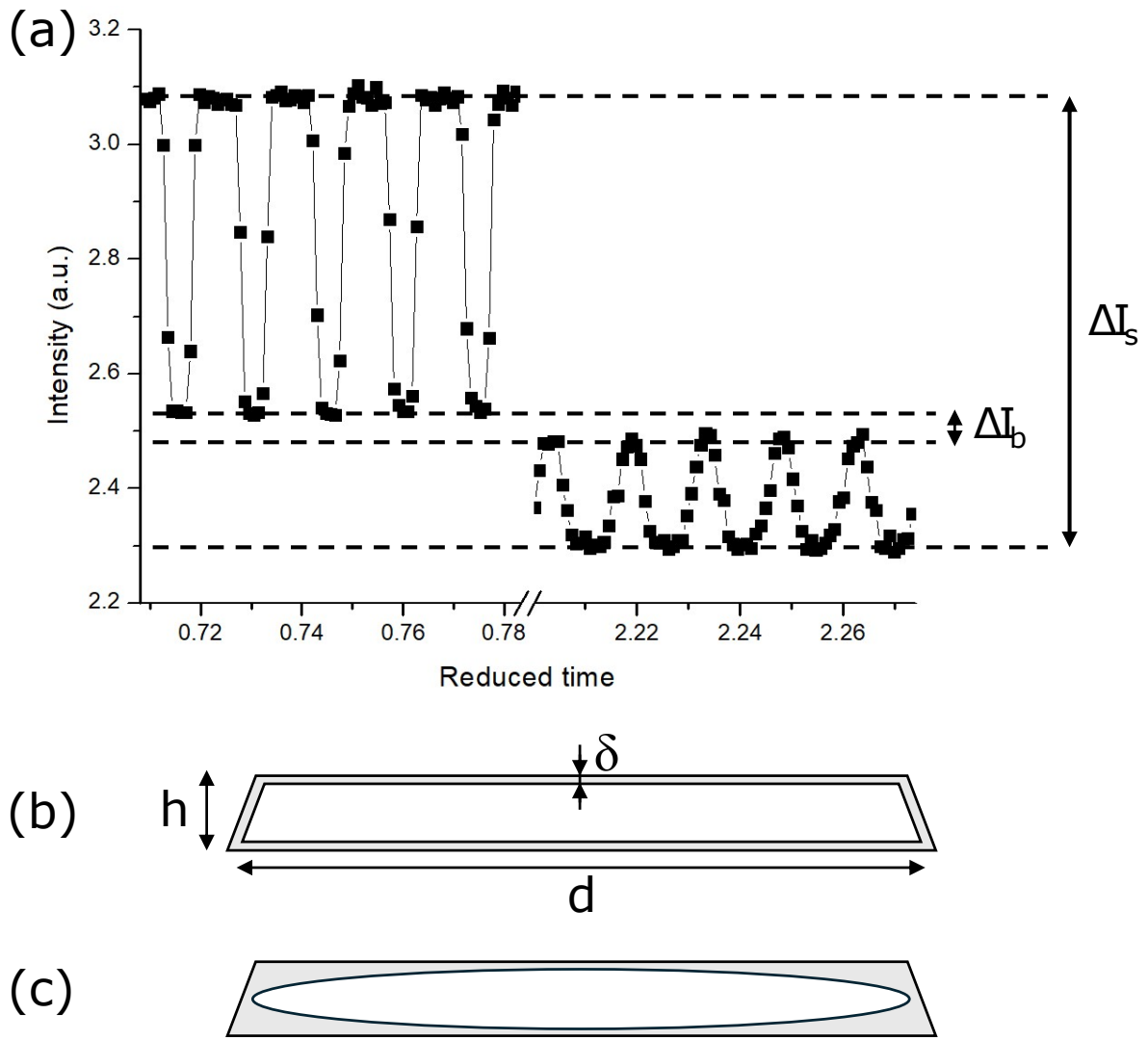
Fig. SI. 5 Evolution of transmitted light intensity as a function of reduced time for segmented flows with argon and pure ethanol ($t_{red}<0.8$) *vs* argon and MB solution ($t_{red}>2$) (a). The difference of intensity was used to calculate the mean film thickness δ using a simple geometrical model (b, cut view of the channel). The most probable shape of the interface is shown as a reference (c). Geometrical parameters are reported for clarity. Grey: liquid phase, white: gas phase.

4 Illustrative images of segmented flows obtained without plasma

(a) Q_g/Q_l =   0.20   5.00   (b)   w/d =

Dichloromethane

Dimethylsulfoxide

Ethanol

0.25

0.50

0.75
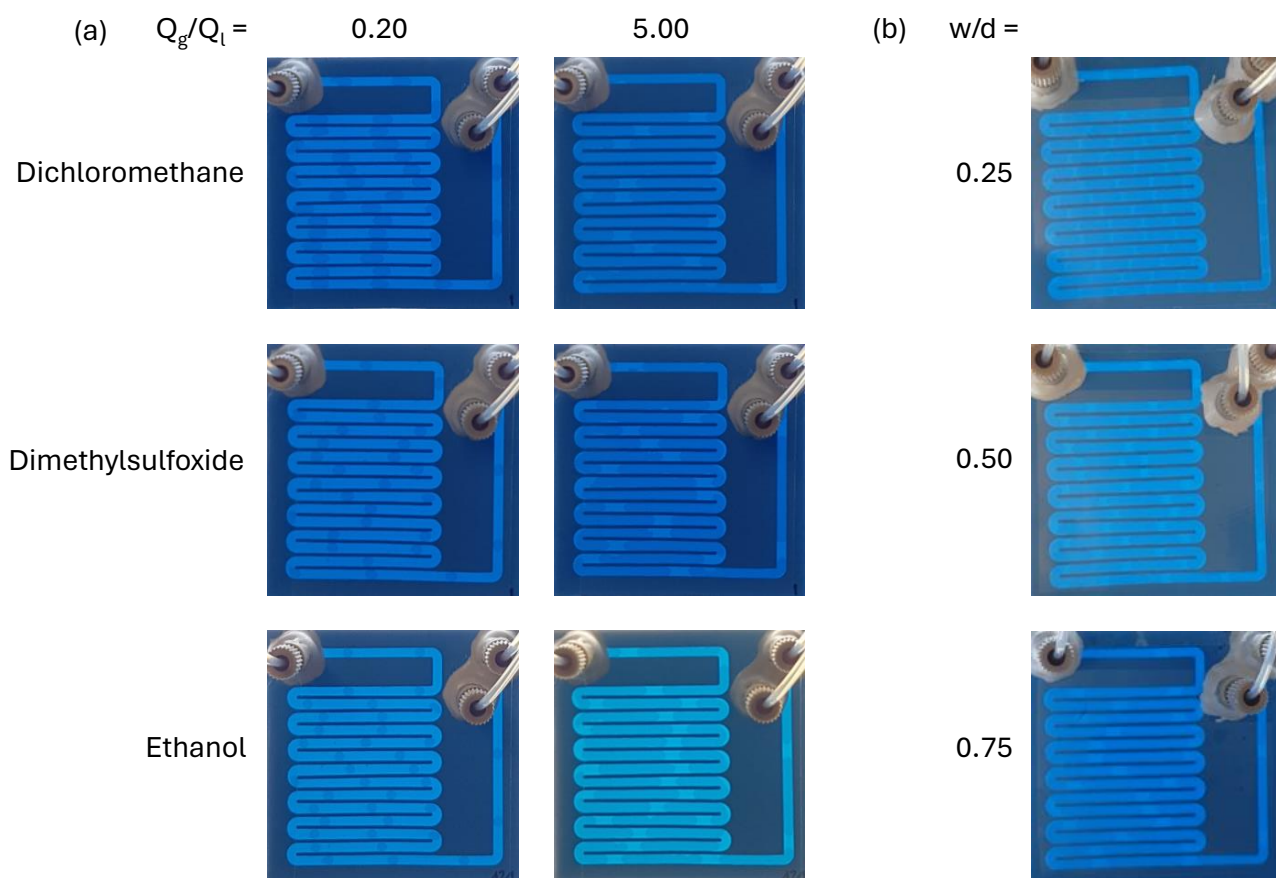
Fig. SI. 6 Images of segmented flows generated in this study for different solvents and at different Q_g/Q_l without plasma (a). In the case of argon-ethanol segmented flows, the effect of the gas entry width is also depicted (b).

5   Scaling laws verification for bubble and slug lengths
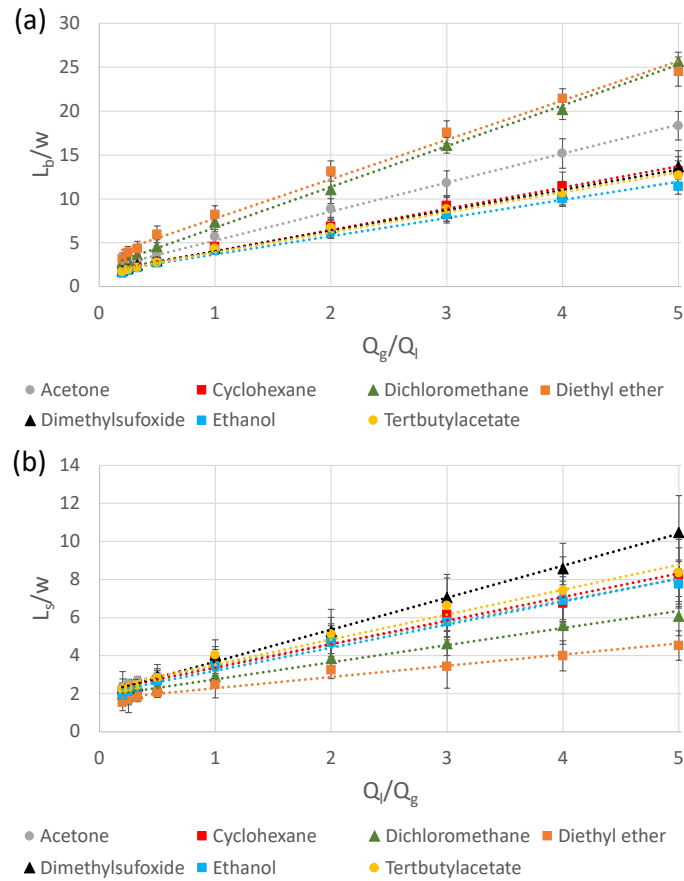
Fig. SI. 7 Evolution of L_b/w (a) and L_s/w (b) as a function of Q_g/Q_l and Q_l/Q_g respectively for gas-liquid segmented flows generated with argon and different liquids.

6 Interfacial area measurements

A gas entry width w of 1.84 mm was used for all experiments except the ones where the effect of w on bubble and slug lengths, and interfacial area was investigated (w was then modified from 0.46 mm to 1.84 mm with all other geometrical parameters unchanged). The bubble surface S_b was computed using the bubble and slug lengths assuming an elliptic cylinder bubble body shape and symmetric ellipsoid caps[3]. As defined in Equations (1) and (2), it included the bubble surface in contact with both the lubrication film and the slugs. The interfacial area A_i was calculated by normalizing the bubble surface to the unit cell volume V_{uc} defined in Equation (3).

$$S_b = \pi \left(\frac{3}{4}(d+h) - \sqrt{d \cdot h} \right) (L_b - h) + \frac{\pi d^2}{2} + \frac{\pi h^2}{4e} ln \left(\frac{1+e}{1-e} \right) \tag{1}$$

$$e^2 = 1 - \frac{h^2}{d^2} \tag{2}$$

$$V_{uc} = (L_b + L_s) \cdot h \cdot d \tag{3}$$

Fig. SI. 8 Evolution of L_b/w (a) and interfacial area (b) as a function of Q_g^*/Q_l^* for different w/d for argon-ethanol segmented flows.

7   Single phase approximation verification for bubble residence time

Fig. SI. 9 Evolution of bubble residence time τ_b as a function of $1/Q_{TP}$ for gas-liquid segmented flows generated with argon and different liquids.
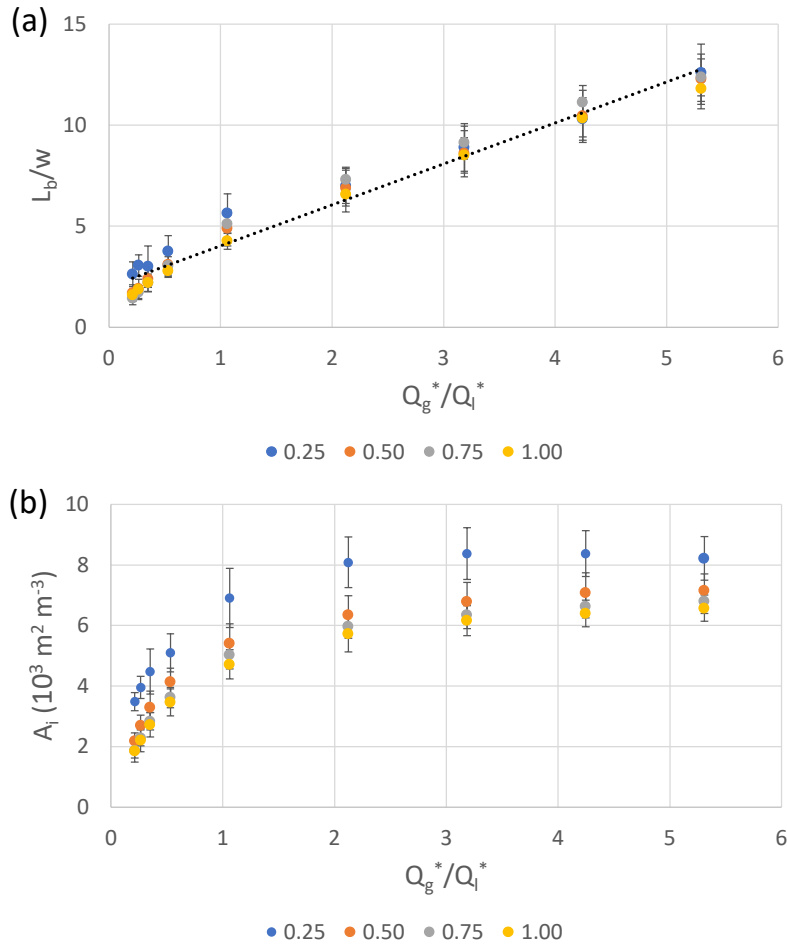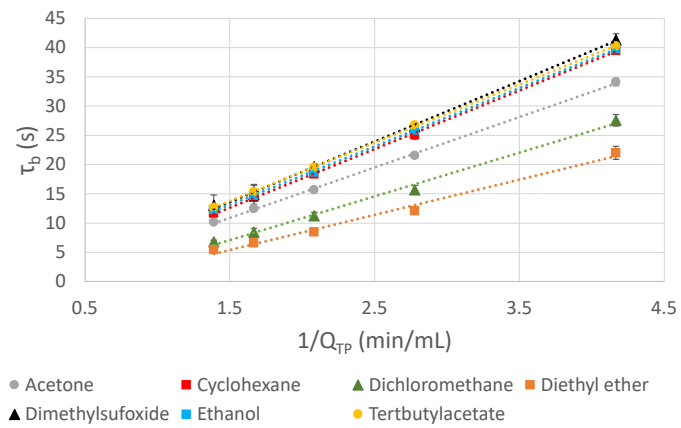
8 Raw experimental data

Table SI. 1 Raw data related to the evolution of L_b/w as a function of Q_g/Q_l for segmented flows generated with argon and the different liquids used (Figure SI.7a).

Q_g/Q_l	0.20	0.25	0.33	0.50	1.00	2.00	3.00	4.00	5.00
1,4-dioxane	1.9±0.3	2.2±0.2	2.5±0.2	3.1±0.3	4.7±0.4	6.9±1.0	9.2±1.2	10.9±1.4	12.9±1.5
Acetone	2.3±0.2	2.5±0.3	3.0±0.2	3.7±0.5	5.7±0.8	8.8±1.2	11.8±1.4	15.2±1.7	18.3±1.6
Acetonitrile	2.3±0.3	2.5±0.3	2.9±0.3	3.6±0.3	5.4±0.9	7.6±1.3	10.3±1.3	13.0±1.3	15.3±1.6
Cyclohexane	1.7±0.2	1.9±0.2	2.2±0.2	2.8±0.3	4.5±0.4	6.8±1.0	9.2±1.1	11.4±1.6	13.2±1.6
Dichloromethane	2.8±0.3	3.0±0.3	3.6±0.4	4.5±0.8	7.4±1.1	11.0±1.6	16.1±0.9	20.2±3.0	25.6±1.1
Diethylether	3.2±0.7	3.9±0.7	4.4±0.8	6.0±0.9	8.2±1.0	13.2±1.1	17.6±1.3	21.4±1.1	24.5±3.0
Dimethylsulfoxide	1.9±0.2	2.1±0.2	2.4±0.3	2.9±0.2	4.4±0.6	6.7±0.9	8.4±1.1	10.6±1.4	13.7±1.8
Dodecane	1.4±0.2	1.6±0.2	1.9±0.2	2.5±0.2	3.9±0.5	6.0±0.8	8.1±1.1	9.8±1.2	11.3±1.0
Ethanol	1.5±0.2	1.8±0.2	2.1±0.2	2.7±0.3	4.1±0.4	6.3±0.8	8.2±0.8	10.0±0.8	11.4±0.9
Ethylacetate	2.0±0.2	2.2±0.2	2.6±0.2	3.1±0.3	4.9±0.6	7.1±1.2	9.5±1.4	11.8±1.4	13.6±1.7
Methanol	2.0±0.2	2.3±0.2	2.6±0.2	3.4±0.5	4.9±0.9	7.4±1.1	9.9±1.4	12.4±1.0	13.8±1.4
Tertbutylacetate	1.7±0.2	1.9±0.2	2.2±0.2	2.8±0.3	4.3±0.4	6.7±1.2	8.8±1.4	10.6±1.3	12.7±1.6
Tetrahydrofurane	2.1±0.2	2.4±0.2	2.6±0.3	3.3±0.2	5.3±0.4	7.7±0.9	10.2±1.1	13.2±1.5	15.6±1.6
Tetrahydropyrane	1.8±0.2	2.1±0.3	2.4±0.2	3.2±0.4	4.7±0.7	7.2±1.1	9.7±1.1	11.9±1.5	13.9±1.5
Toluene	1.8±0.2	2.1±0.2	2.4±0.3	3.0±0.9	4.0±1.7	6.0±2.1	7.4±1.6	10.5±2.6	13.0±1.7

Table SI. 2 Raw data related to the evolution of L_s/w as a function of Q_l/Q_g for segmented flows generated with argon and the different liquids used (Figure SI.7b).

Q_l/Q_g	0.20	0.25	0.33	0.50	1.00	2.00	3.00	4.00	5.00
1,4-dioxane	2.2±0.2	2.3±0.2	2.6±0.3	2.9±0.3	3.9±0.6	5.4±0.7	6.5±0.9	7.8±1.2	9.0±1.6
Acetone	2.4±0.8	2.5±0.2	2.7±0.2	2.9±0.4	3.7±0.6	4.7±0.9	5.9±1.1	7.0±1.2	7.8±1.1
Acetonitrile	2.4±0.3	2.6±0.3	2.7±0.3	3.0±0.4	4.1±0.5	5.5±0.9	6.7±1.1	7.9±1.1	8.7±1.4
Cyclohexane	2.1±0.2	2.2±0.3	2.5±0.3	2.7±0.3	3.7±0.4	4.8±0.9	6.2±0.8	6.7±1.0	8.2±1.4
Dichloromethane	2.0±0.3	1.9±0.9	2.0±0.3	2.3±0.3	2.9±0.5	3.9±0.6	4.6±0.6	5.6±1.0	6.1±1.0
Diethylether	1.5±0.4	1.7±0.3	1.8±0.2	2.1±0.3	2.5±0.7	3.3±0.5	3.4±1.2	4.0±0.8	4.5±0.8
Dimethylsulfoxide	2.3±0.5	2.3±0.3	2.4±0.2	2.9±0.3	4.0±0.4	5.3±0.7	7.1±1.0	8.6±1.3	10.5±1.9
Dodecane	2.0±0.2	2.1±0.2	2.4±0.3	2.7±0.3	3.5±0.4	4.8±0.7	6.3±1.1	7.3±1.2	8.4±1.5
Ethanol	1.9±0.3	2.1±0.2	2.3±0.2	2.7±0.3	3.5±0.5	4.7±0.6	5.8±0.8	6.9±1.0	7.8±1.3
Ethylacetate	2.3±0.2	2.4±0.3	2.6±0.4	2.9±0.3	3.8±0.7	5.0±0.9	6.4±1.1	7.4±1.2	8.6±1.6
Methanol	2.1±0.3	2.3±0.3	2.5±0.3	2.7±0.7	3.5±0.8	5.0±0.8	6.0±0.8	7.2±1.1	8.1±1.2
Tertbutylacetate	2.2±0.4	2.3±0.4	2.5±0.4	2.8±0.7	4.0±0.8	5.1±1.3	6.6±1.6	7.4±1.8	8.3±1.8
Tetrahydrofurane	2.2±0.2	2.3±0.2	2.5±0.2	2.8±0.6	3.9±0.5	5.1±0.7	6.6±1.0	7.4±1.0	8.6±1.2
Tetrahydropyrane	2.2±0.2	2.3±0.2	2.5±0.3	2.9±0.3	4.0±0.6	5.2±0.8	6.5±1.1	7.7±1.3	8.5±1.6
Toluene	2.2±0.3	2.3±0.3	2.6±0.7	3.1±0.8	3.8±0.9	5.5±2.1	6.1±1.0	7.2±1.5	8.3±1.9

Table SI. 3 Correlation between Q_g/Q_l and Q_g^*/Q_l^* for the different liquids used (Figure 3).

Qg/Ql	0.20	0.25	0.33	0.50	1.00	2.00	3.00	4.00	5.00
1-4-dioxane	0.21	0.26	0.34	0.52	1.04	2.08	3.12	4.16	5.20
Acetone	0.27	0.33	0.44	0.66	1.33	2.65	3.98	5.30	6.63
Acetonitrile	0.22	0.28	0.36	0.55	1.10	2.21	3.31	4.41	5.52
Cyclohexane	0.22	0.28	0.37	0.56	1.12	2.23	3.35	4.46	5.58
Dichloromethane	0.38	0.47	0.62	0.94	1.88	3.77	5.65	7.53	9.42
Diethylether	0.48	0.60	0.79	1.20	2.40	4.81	7.21	9.62	12.02
Dimethylsulfoxide	0.20	0.25	0.33	0.50	1.00	2.00	3.00	4.00	5.00
Dodecane	0.20	0.25	0.33	0.50	1.00	2.00	3.00	4.00	5.00
Ethanol	0.21	0.27	0.35	0.53	1.06	2.12	3.19	4.25	5.31
Ethylacetate	0.22	0.28	0.37	0.55	1.11	2.22	3.32	4.43	5.54
Methanol	0.23	0.29	0.38	0.57	1.15	2.30	3.45	4.60	5.75
Terbutylacetate	0.21	0.27	0.35	0.53	1.07	2.13	3.20	4.27	5.33
Tetrahydrofurane	0.24	0.30	0.40	0.60	1.20	2.41	3.61	4.82	6.02
Tetrahydropyrane	0.22	0.28	0.36	0.55	1.10	2.21	3.31	4.42	5.52
Toluene	0.21	0.26	0.34	0.51	1.03	2.06	3.09	4.12	5.15

Table SI. 4 Raw data related to the evolution of L_b/w as a function of Q_g/Q_l and w/d for argon-ethanol segmented flows (Figure SI.8a).

Qg/Ql	0.20	0.25	0.33	0.50	1.00	2.00	3.00	4.00	5.00
0.25	2.6 ± 0.6	3.1 ± 0.5	3.0 ± 1.0	3.7 ± 0.8	5.6 ± 1.0	7.0 ± 0.9	8.9 ± 1.2	10.3 ± 1.1	12.6 ± 1.4
0.50	1.7 ± 0.4	1.9 ± 0.5	2.4 ± 0.6	3.1 ± 0.6	4.9 ± 0.9	6.9 ± 0.9	8.6 ± 1.1	10.4 ± 1.3	12.3 ± 1.2
0.75	1.4 ± 0.3	1.7 ± 0.4	2.2 ± 0.4	3.0 ± 0.5	5.1 ± 0.7	7.3 ± 0.6	9.1 ± 0.8	11.1 ± 0.8	12.4 ± 0.9
1.00	1.6 ± 0.2	1.9 ± 0.2	2.2 ± 0.2	2.8 ± 0.3	4.3 ± 0.4	6.6 ± 0.9	8.5 ± 0.9	10.3 ± 0.9	11.8 ± 1.0

Table SI. 5 Raw data related to the evolution of interfacial area A_i (10^3 m^2 m^{-3}) as a function of Q_g/Q_l and w/d for argon-ethanol segmented flows (Figure SI.8b).

Qg/Ql	0.20	0.25	0.33	0.50	1.00	2.00	3.00	4.00	5.00
0.25	3.5 ± 0.3	4.0 ± 0.4	4.5 ± 0.8	5.1 ± 0.6	6.9 ± 1.0	8.1 ± 0.8	8.4 ± 0.9	8.4 ± 0.8	8.2 ± 0.7
0.50	2.2 ± 0.3	2.7 ± 0.3	3.3 ± 0.5	4.1 ± 0.5	5.4 ± 0.6	6.4 ± 0.6	6.8 ± 0.6	7.1 ± 0.7	7.2 ± 0.6
0.75	1.9 ± 0.2	2.3 ± 0.3	2.8 ± 0.3	3.6 ± 0.3	5.0 ± 0.5	6.0 ± 0.4	6.4 ± 0.5	6.6 ± 0.4	6.8 ± 0.4
1.00	1.9 ± 0.4	2.2 ± 0.4	2.7 ± 0.4	3.5 ± 0.4	4.7 ± 0.5	5.7 ± 0.6	6.2 ± 0.5	6.4 ± 0.4	6.6 ± 0.4

Table SI. 6 Raw data related to the evolution of bubble residence time τ_b (s) as a function of $1/Q_{TP}$ for the different liquids used (Figure SI.9).

$1/Q_{TP}$ (min/mL)	1.4	1.7	2.1	2.8	4.2
1,4-dioxane	12.6±0.8	15.2±1.0	19.3±0.4	26.2±0.4	39.8±0.6
Acetone	10.1±0.3	12.5±0.3	15.7±0.3	21.6±0.4	34.1±0.6
Acetonitrile	11.7±0.2	14.2±0.3	17.9±0.2	24.4±0.2	37.3±0.6
Cyclohexane	11.7±1.3	14.4±2.2	18.4±0.3	25.1±0.7	39.5±0.6
Dichloromethane	6.8±0.3	8.5±0.6	11.2±0.6	15.7±0.7	26.8±1.0
Diethylether	5.4±0.5	6.6±0.5	8.5±0.3	12.1±0.5	22.0±1.1
Dimethylsulfoxide	13.7±1.8	15.3±1.6	19.7±0.5	26.5±0.3	41.3±1.0
Dodecane	12.9±0.3	15.0±0.3	19.7±0.3	26.5±0.3	41.8±0.7
Ethanol	12.3±0.3	14.7±0.3	18.7±0.3	25.9±0.7	39.8±0.6
Ethylacetate	12.4±0.3	14.9±0.2	18.9±0.3	25.1±0.3	39.1±0.6
Methanol	11.4±0.3	13.8±0.2	17.5±0.4	24.0±0.3	36.6±0.4
Tertbutylacetate	12.7±0.2	15.4±0.5	19.5±0.3	26.7±0.3	40.3±0.6
Tetrahydrofurane	11.3±0.3	13.8±0.2	17.5±0.2	23.8±0.2	37.5±0.6
Tetrahydropyrane	12.1±0.4	14.9±1.2	19.1±0.5	26.3±0.5	40.4±0.7
Toluene	13.1±0.2	15.7±0.3	21.0±2.0	28.0±1.2	39.8±1.9

Table SI. 7 Raw data related to the evolution of mean reduced time θ and film thickness δ (μm) as a function of Q_g/Q_l for argon-ethanol segmented flows (Figure 5).

Q_g/Q_l	θ	δ (μm)
5.00	1.59	12 ± 4
4.00	1.45	11 ± 4
3.00	1.36	9 ± 4
2.00	1.22	6 ± 4
1.00	1.09	8 ± 4
0.50	1.11	20 ± 6
0.33	1.13	19 ± 7
0.25	1.14	22 ± 9
0.20	1.14	30 ± 7

Table SI. 8 Raw data related to the evolution of flow pattern as a function of plasma power P (W) and liquid boiling point T_{eb} (K) for segmented flows generated with argon and different liquids used (Figure 7).

Liquid	T_{eb} (K)	P (W)			Flow pattern		
		5.0 kV	10.0 kV	15.0 kV	5.0 kV	10.0 kV	15.0 kV
Acetone	329	1.18	3.79	7.29	Elongated	Elongated	Annular
Acetonitrile	355	1.21	2.81	4.53	Elongated	Elongated	Elongated
Cyclohexane	354	1.60	5.19	9.12	Elongated	Elongated	Annular
Dichloromethane	313	1.33	4.72	10.08	Elongated	Annular	Vaporized
Diethylether	308	1.45	6.42	11.62	Elongated	Vaporized	Vaporized
Dimethylsulfoxide	462	0.68	2.34	4.00	Elongated	Elongated	Elongated
Dodecane	489	1.49	4.34	8.15	Elongated	Elongated	Elongated
Ethanol	352	1.08	2.88	4.97	Elongated	Elongated	Elongated
Ethylacetate	350	1.79	5.88	10.95	Elongated	Annular	Annular
Methanol	338	0.88	1.82	2.68	Elongated	Elongated	Elongated
Tertbutylacetate	371	1.73	5.45	10.84	Elongated	Annular	Annular
Tetrahydrofurane	339	1.73	5.53	9.97	Elongated	Annular	Annular

Table SI. 9 Raw data related to the evolution of breakdown voltage U_c (kV) as a function of $\beta = \frac{Q_g}{Q_g+Q_l}$ for argon-ethanol segmented flows (Figure 8).

β	U_c (kV)
0.25	5.0 ± 0.5
0.33	4.4 ± 0.4
0.50	4.0 ± 0.4
0.67	3.2 ± 0.3
0.75	2.6 ± 0.3
0.80	2.2 ± 0.2
0.83	2.0 ± 0.2
1.00	1.4 ± 0.1

Table SI. 10 Raw data related to the evolution of plasma power P (W) and specific input energy (SEI, J mL^{-1}) as a function of Q_g/Q_l and voltage applied (kV) for argon-ethanol segmented flows (Figure 9).

Q_g/Q_l	Voltage (kV)	0.25	0.33	0.50	1.00	2.00	3.00	4.00	5.00
	5.0	0.19	0.32	0.60	0.95	1.04	1.10	1.12	1.08
	7.5	0.40	0.70	1.18	1.73	1.94	2.04	1.98	1.95
P (W)	10.0	0.61	1.28	1.96	2.69	2.83	3.03	2.96	2.88
	12.5	0.96	1.90	2.93	3.76	3.89	4.00	3.82	3.78
	15.0	1.51	2.93	3.92	4.76	4.81	4.91	4.84	4.97
	5.0	0.03	0.04	0.08	0.13	0.07	0.05	0.04	0.03
	7.5	0.06	0.10	0.16	0.24	0.13	0.09	0.07	0.05
P (W)	10.0	0.08	0.18	0.27	0.37	0.20	0.14	0.10	0.08
	12.5	0.13	0.26	0.41	0.52	0.27	0.19	0.13	0.11
	15.0	0.21	0.41	0.54	0.66	0.33	0.23	0.17	0.14

Table SI. 11 Raw data related to the evolution of bubble residence time normalized to bubble residence time without plasma τ_b^{pl}/τ_b and relative bubble length increase $(L_b^{out}-L_b^{in})/L_b^{in}$ as a function of Q_g/Q_l and voltage applied (kV) for argon-ethanol segmented flows (Figure 10).

Voltage (kV)	Q_g/Q_l	0.25	0.33	0.50	1.00	2.00	3.00	4.00	5.00
	5.0	1.00±0.01	0.98±0.01	0.89±0.01	0.56±0.04	0.65±0.01	0.66±0.01	0.69±0.01	0.73±0.01
	7.5	0.98±0.01	0.90±0.01	0.75±0.01	0.46±0.00	0.50±0.01	0.52±0.01	0.55±0.01	0.62±0.02
τ_b^{pl}/τ_b	10.0	0.97±0.01	0.78±0.01	0.62±0.01	0.34±0.01	0.38±0.00	0.41±0.00	0.44±0.01	0.49±0.04
	12.5	0.93±0.01	0.68±0.01	0.47±0.00	0.25±0.00	0.30±0.01	0.32±0.01	0.34±0.01	0.36±0.01
	15.0	0.85±0.02	0.55±0.01	0.37±0.01	0.18±0.01	0.22±0.01	0.24±0.01	0.26±0.01	0.27±0.01
	No plasma	15	10	10	10	10	10	13	17
	5.0	0	8	10	170	125	99	60	65
$(L_b^{out}-L_b^{in})/L_b^{in}$	7.5	0	0	32	357	270	175	139	116
	10.0	2	0	295	628	367	307	237	197
	12.5	14	38	581	929	533	418	298	268
	15.0	15	464	963	1373	799	599	500	424

References

1 M. Holub, *International Journal of Applied Electromagnetics and Mechanics*, 2012, **39**, 81–87.

2 J. Villermaux, *Génie de la réaction chimique : Conception et fonctionnement des réacteurs*, 2nd edn., 1995.

3 C. Zhu, C. Li, X. Gao, Y. Ma and D. Liu, *International Journal of Heat and Mass Transfer*, 2014, **73**, 492–499.